Ring current dynamics in moderate and strong storms: Comparative analysis of TWINS and IMAGE/HENA data with the Comprehensive Ring Current Model

N. Buzulukova,[1] M.-C. Fok,[1] J. Goldstein,[2,3] P. Valek,[2,3] D. J. McComas,[2,3] and P. C. Brandt[4]

Received 19 January 2010; revised 30 September 2010; accepted 6 October 2010; published 15 December 2010.

[1] We present a comparative study of ring current dynamics during strong and moderate storms. The ring current during the strong storm is studied with IMAGE/HENA data near the solar cycle maximum in 2000. The ring current during the moderate storm is studied using energetic neutral atom (ENA) data from the Two Wide-Angle Imaging Neutral-Atom Spectrometers (TWINS) mission during the solar minimum in 2008. For both storms, the local time distributions of ENA emissions show signatures of postmidnight enhancement (PME) during the main phases. To model the ring current and ENA emissions, we use the Comprehensive Ring Current Model (CRCM). CRCM results show that the main-phase ring current pressure peaks in the premidnight-dusk sector, while the most intense CRCM-simulated ENA emissions show PME signatures. We analyze two factors to explain this difference: the dependence of charge-exchange cross section on energy and pitch angle distributions of ring current. We find that the IMF B_y effect (twisting of the convection pattern due to B_y) is not needed to form the PME. Additionally, the PME is more pronounced for the strong storm, although relative shielding and hence electric field skewing is well developed for both events.

Citation: Buzulukova, N., M.-C. Fok, J. Goldstein, P. Valek, D. J. McComas, and P. C. Brandt (2010), Ring current dynamics in moderate and strong storms: Comparative analysis of TWINS and IMAGE/HENA data with the Comprehensive Ring Current Model, *J. Geophys. Res.*, *115*, A12234, doi:10.1029/2010JA015292.

1. Introduction

[2] A geomagnetic storm is identified through the global deviation of the H component of the geomagnetic field at low latitudes (i.e., the *Dst* index). The main source of substantial negative deviations in the *Dst* index is the ring current (RC) [*Dessler and Parker*, 1959; *Burton et al.*, 1975]. The intensity of storm time RC can be measured by the *Dst* index, with corrections for pressure, quiet time offset, and shielding currents.

[3] Despite an unusually low level of geomagnetic activity during 2008, there are a number of moderate storms with deviations in the *Dst* of ~−60 nT. Energetic neutral atom (ENA) images of the RC during these moderate storms are successfully captured by the TWINS (Two Wide-Angle Imaging Neutral-Atom Spectrometers) mission [*McComas et al.*, 2009]. The first stereoscopic ENA images from TWINS during the moderate storm of 15 June 2008 confirm that the RC plasma is highly asymmetric during the main phase [*McComas et al.*, 2009].

[4] There is an important unresolved issue in RC asymmetry. Analysis of the asymmetric part of H component shows that the RC pressure exhibits strong asymmetry during the main phase of a storm, but where the pressure peak is located is not completely understood. Traditionally, the bulk of the RC pressure is thought to be concentrated in the dusk sector, based on ground-based measurements of H variation [e.g., *Shi et al.*, 2006]. Statistical studies of magnetic depression maps of the inner magnetosphere acquired with CRRES, ISEE, AMPTE/CCE and Polar mission also show that the peak of the partial RC is located in the dusk sector [*Le et al.*, 2004; *Jorgensen et al.*, 2004]. The same result is obtained by *Anderson et al.* [2005] from analysis of Iridium data. This point of view is supported by RC modeling with a dipole magnetic field and Volland-Stern electric field [*Ebihara et al.*, 2002].

[5] This traditional picture is called into question by new findings from IMAGE mission. ENA images from the IMAGE/HENA instrument show that ion fluxes during the main phase of storms often peak near midnight and sometimes near the postmidnight sector [*Brandt et al.*, 2002]. This surprising asymmetry in RC plasma is attributed to eastward skewing of the convection electric field and called

[1]NASA Goddard Space Flight Center, Greenbelt, Maryland, USA.
[2]Space Science and Engineering Division, Southwest Research Institute, San Antonio, Texas, USA.
[3]Department of Physics and Astronomy, University of Texas at San Antonio, San Antonio, Texas, USA.
[4]Applied Physics Laboratory, Johns Hopkins University, Laurel, Maryland, USA.

Copyright 2010 by the American Geophysical Union.
0148-0227/10/2010JA015292

postmidnight enhancement (PME). Two factors are proposed by *Brandt et al.* [2002] to explain the skewing: (1) shielding electric fields created by the RC and (2) the IMF B_y effect.

[6] The storm time RC reorganization of the inner magnetosphere electric field includes (among other effects): shielding of the outer convection electric field inside the equatorward RC boundary; formation of a strong electric field in the evening sector; and, skewing of the whole nightside potential pattern. These results are demonstrated by numerous modeling calculations [*Jaggi and Wolf*, 1973; *Harel et al.*, 1981; *Toffoletto et al.*, 2003; *Garner et al.*, 2004] and analysis of experimental data [*Burke et al.*, 1998; *Rowland and Wygant*, 1998; *Wygant et al.*, 1998; *Burke et al.*, 2000; *Nishimura et al.*, 2009]. Observationally, storm time electric fields in the inner magnetosphere may be more intense than the outer convection field. The intense electric fields are associated with southward IMF B_z rather than with strong IMF B_y. The observed intense electric fields and associated skewing are the result of RC-induced changes in the potential pattern.

[7] *Fok et al.* [2003] examine a PME in ENA data. They model the event with both the Weimer convection model and with the Comprehensive Ring Current Model (CRCM). CRCM electric field exhibits strong skewing, and ion fluxes produce a clear PME. CRCM-simulated ENA fluxes peak in the dawn sector and show very good agreement with IMAGE/HENA data. Weimer-simulated ENA distributions peak in the dusk sector. *Fok et al.* [2003] attribute the strong skewed electric field and PME to a twisting of equipotentials arising from shielding effects and an ionospheric conductivity gradient near the terminator. *Ebihara and Fok* [2004] study several strong storms with clear PME signatures for 39–50 keV in IMAGE/HENA data and model them with the CRCM. They find that PME are common for RC distributions during strong storms. The main factor that controls PME is the shielding effect. The effect of B_y is not considered. *Liemohn et al.* [2005] conclude that RC models with RC-induced electric fields reproduce ENA emissions better than simple models using the Volland-Stern convection model.

[8] *Denton et al.* [2005] show that MENA/IMAGE ENA data for 6 keV and a corresponding modeled image are in good agreement. The modeled image is obtained with Volland-Stern electric field. No PME is reported. *Denton et al.* [2005] note that the peak location depends on energy, a dependence that requires further investigation.

[9] *Ebihara and Fok* [2004] and *Lavraud et al.* [2008] suggest how to obtain PME in the absence of electric field skewing. The RC source should be located in the postmidnight sector. This forms a PME in both Weimer and Volland-Stern convection models. In the case of such unusual distributions of the source, PME may form only for middle to low energies (tens of keV and below) and the total contribution from this population to total RC energy should be small [*Lavraud et al.*, 2008]. However, the analysis of *Lavraud et al.* [2008] does not include any ENA data.

[10] *Lui* [2003] points out that statistical results from in situ particle measurements [e.g., *Le et al.*, 2004] do not agree with an ENA peak in the postmidnight or dawn sectors. As possible explanations of that result, *Lui* [2003] proposes that (1) PME may be short-lived phenomenon, and the statistical study of *Le et al.* [2004] does not resolve them, (2) ENA measurements cover only a limited range of energies, and (3) a pitch angle anisotropy of the distribution function may play an important role.

[11] In this study we try to resolve the questions raised by *Lui* [2003] and analyze the relationship between the partial RC pressure and ENA emissions. We use ENA emissions acquired with TWINS to analyze a moderate storm near solar minimum in 2008, and IMAGE/HENA data for a strong storm near solar maximum in 2000. We use the CRCM to model RC dynamics, calculate 3-D ion H^+ fluxes, and reconstruct ENA emissions. Several questions are addressed: (1) What range of ion energies form ENA PME? (2) What range of ion energies contribute to the bulk of RC pressure? (3) Where is the pressure peak located? (4) How are these characteristics affected by the size of the storm? (5) What is the effect of IMF B_y on PME? (6) What is the effect of RC pitch angle anisotropy on PME?

[12] Both storms satisfy the criterion of *Brandt et al.* [2002], i.e., with $Dst_{\min} < -50$ nT. They have different spectral characteristics of a PME and different RC morphology though. Also, we are able to examine the PME from two different vantage points by taking advantage of the stereo viewing offered by TWINS.

2. The 11 October 2008 Event: TWINS Data

[13] As an example of a moderate storm, we chose the 11 October 2008 event, a moderate CIR-driven storm near solar minimum with $Dst_{\min} = -60$ nT. Figure 1 shows the solar wind (SW), interplanetary magnetic field (IMF) data, and geomagnetic conditions for this event. Early on 11 October, activity is minimal. The main phase of the storm starts around 0800 UT with a sharp *AL* intensification around 0815 UT and reaches $Dst_{\min}$ around 1100 UT.

[14] Figures 2 and 3 show TWINS 1 and TWINS 2 "fish-eye" stereo ENA images of the ring current and precipitating ions around 1000 UT (left column) and 1030 UT (right column) for 8 keV (top row) and 12 keV (bottom row). It is assumed the ENA are hydrogen emissions. Each image is calculated with ~15 min exposure to accumulate sufficient statistics. For reference, dipole magnetic field lines are shown at L = 4 and L = 8, with 1200 magnetic local time (MLT) (noon) in red, 1800 MLT (dusk) in magenta, 2400 MLT (midnight), and 0600 MLT (dawn) in white. The black sectors in the TWINS 1 data are marked owing to a bright background from viewing toward the Sun. A detailed description of TWINS imagers can be found in work by *McComas et al.* [2009].

[15] The highest ENA intensities observed by TWINS 2 come from pixels located near the Earth limb. These so-called low-altitude (LA) emissions originate from the interaction of precipitating ions with the oxygen exobase. RC emissions may be considered as optically thin, while LA emissions are optically thick. LA emissions are very localized, but the scattering of ENA in the carbon foils inside the TWINS detectors causes spreading of the LA emission signal between different pixels along the polar angle direction. In this work, we do not perform quantitative analysis of LA emissions. However, bright optically thin RC emissions may be formed in the transition region between LA emis-

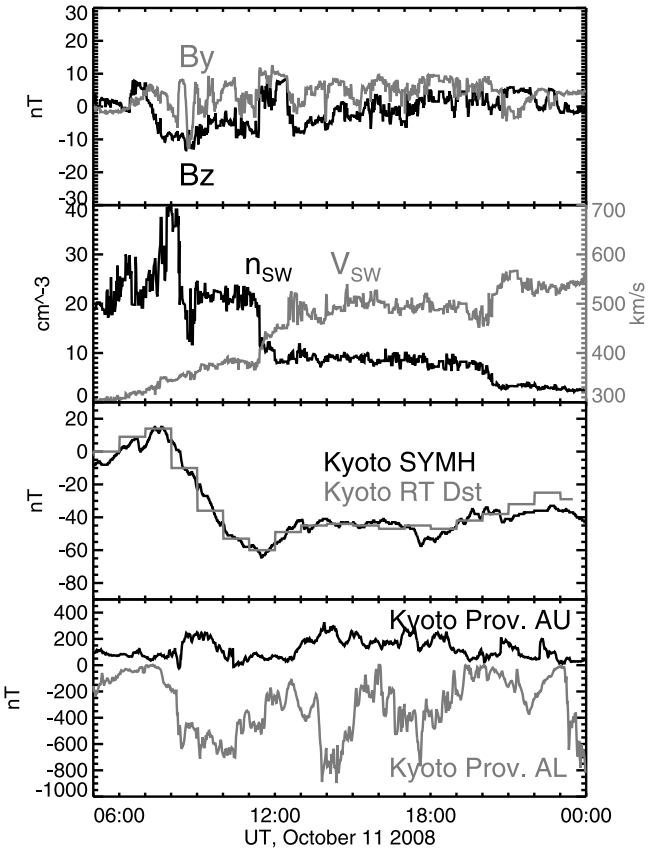

Figure 1. Geomagnetic conditions for 11 October 2008. From top to bottom: IMF B_z and B_y (Advanced Composition Explorer (ACE)); solar wind density and velocity (ACE); *SYMH* and real-time *Dst* (World Data Center for Geomagnetism, Kyoto (hereafter referred to as Kyoto)); and provisional *AU* and *AL* (Kyoto).

sions and high-altitude RC emissions (see section 5). A detailed analysis of LA emissions for 11 October 2008 is done by *Bazell et al.* [2010].

[16] RC emissions at TWINS 1 and TWINS 2 are seen as regions of enhanced ENA fluxes at <3 R_E, predominantly in the postmidnight-to-dawn sector. In the TWINS 2 data, RC emissions partly overlap with the LA emissions. Due to the difference in viewing geometries between the two spacecrafts, LA emissions in TWINS 1 are much less intense. Additionally, ENA fluxes at 12 keV are less intense than at 8 keV for both TWINS 1 and TWINS 2 images. We find that the ENA flux spectra in these images monotonically decrease with energy starting from ~5 keV. RC ENA emissions are relatively stable from 1000 to 1030 UT on 11 October 2008 with the same spatial distribution. These data provide an example of a RC PME during the main phase for a moderate storm.

3. The 12 August 2000 Event: IMAGE/HENA Data

[17] The 12 August 2000 event is a strong CME-driven storm near solar maximum with the $Dst_{\min} = -235$ nT occurring at 10 UT. Figure 4 shows SW data, IMF data, and geomagnetic conditions for 11–12 August 2000. This case is chosen as an example of a strong storm because IMAGE/HENA captures clear RC emissions with a PME during the storm main phase. The 12 August 2000 event is studied by *Ebihara et al.* [2004], showing the conductance effect on RC dynamics; by *Ebihara and Fok* [2004], showing PME development at 39–50 keV near the storm main phase; and, by *Buzulukova et al.* [2010], showing the validity of CRCM-MHD coupled model using IMAGE/HENA data. Here we concentrate specifically on the relationship between the PME and pressure peak, the pitch angle anisotropy effect, and the IMF B_y effect.

[18] Figure 5 shows the hydrogen ENA flux intensity in the energy ranges 39–50 keV, 50–60 keV and 60–81 keV, as seen by IMAGE/HENA from a polar vantage point (XYZ s/c SM coordinates are 0.1, 0.5, 6.1 R_E). The projection is the same as for the TWINS data with dipole lines for L = 4, L = 8 drawn for 2400 (white), 0600 (white), 1200 (red), 1800 (magenta) MLT. The sun is located to the left of the image. The data are shown for the main phase of the storm near 09 UT with ~20 min integration time. The maximum of ENA emissions is located in the postmidnight sector for 39–50 keV (and energies below, not shown here); at midnight for 50–60 keV, and around ~23 MLT for 60–81 keV. However, all three energy bins show similar morphology, namely strong ENA fluxes up to ~07 MLT. This structure is typical for PME [*Brandt et al.*, 2002; *Ebihara and Fok*, 2004], indicating ring current asymmetry during the main phase. (It should be noted that 10 of the 18 events considered

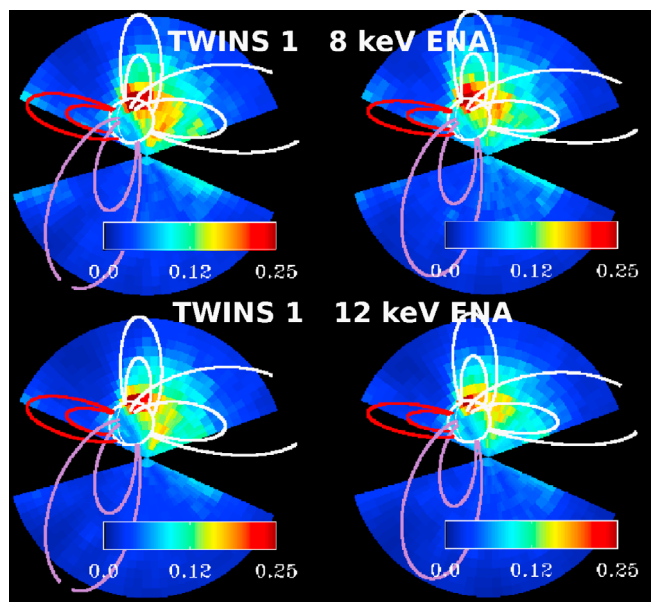

Figure 2. TWINS 1 hydrogen ENA flux intensity (/cm^2/sr/s/eV) in "fish-eye" projection for 11 October 2008 around (left column) 1000 UT and (right column) 1030 UT for (top) 8 keV and (bottom) 12 keV. Dipole magnetic field lines are shown at L = 4 and L = 8, with 1200 MLT (noon) in red, 1800 MLT (dusk) in magenta, and 2400 MLT (midnight) and 0600 MLT (dawn) in white. A linear scale is used for ENA flux intensity. Black sectors are marked owing to a bright background from viewing toward the Sun.

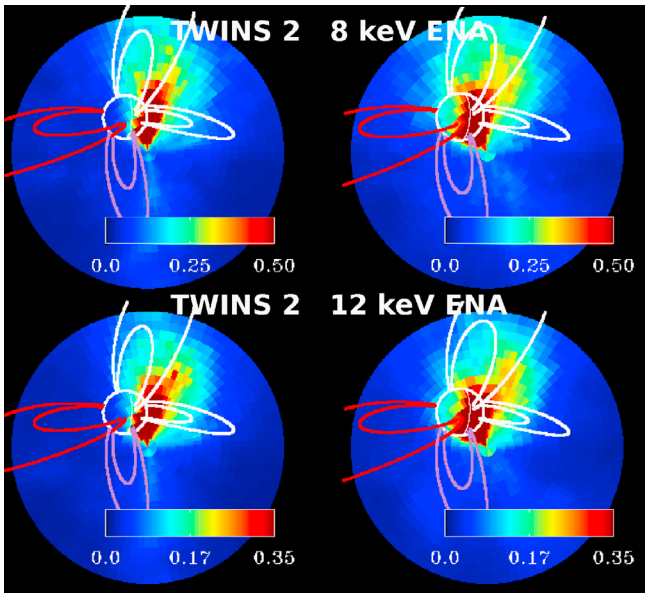

Figure 3. TWINS 2 hydrogen ENA flux intensity (/cm^2/sr/s/eV) for 11 October 2008 around (left column) 1000 UT and (right column) 1030 UT for (top) 8 keV and (bottom) 12 keV. The format is the same as for Figure 2.

by *Brandt et al.* [2002] have an ENA maximum located between 23 and 01 MLT.)

4. Comprehensive Ring Current Model and Input Data

4.1. CRCM Basic Equations

[19] The CRCM [*Fok et al.*, 2001] is used to calculate RC fluxes, RC pressure, electric fields, Region II currents in the inner magnetosphere, and ENA emissions. The CRCM calculates field-aligned currents (FAC) self-consistently with the RC pressure distribution. A self-consistency between the magnetic field and RC pressure, however, is not implemented in this version.

[20] At each time step, the calculations in CRCM are performed in two stages. First, the CRCM solves the bounce-averaged Boltzmann equation to obtain the temporal evolution of the four dimensional phase space density $\bar{f}_s$ (for H^+ and O^+). The phase space density is specified by two ionospheric coordinates (invariant latitude λ and magnetic local time ϕ) and two adiabatic invariants (relativistic magnetic moment M and invariant K related to the second adiabatic invariant J by $K = J/\sqrt{8m_0M}$ where m_0 is a rest mass of corresponding ion). Taking into account particle drift and losses, the bounce-averaged Boltzmann equation is

$$\frac{\partial \bar{f}_s}{\partial t} + \langle \dot{\lambda} \rangle \frac{\partial \bar{f}_s}{\partial \lambda} + \langle \dot{\phi} \rangle \frac{\partial \bar{f}_s}{\partial \phi} = -\mathrm{v}\sigma_s \langle \mathrm{n_H} \rangle \bar{f}_s - \left(\frac{\bar{f}_s}{0.5\tau_b} \right)_{loss\ cone} \quad (1)$$

where the operator $\langle \ldots \rangle$ means bounce-averaged, v is a particle velocity, σ_s is a cross section for charge-exchange losses with the geocorona, $\mathrm{n_H}$ is a geocoronal H density, and τ_b is a bounce period. The last term is calculated only for particles that populate the loss cone. The expressions for bounce-averaged velocities $\langle \dot{\lambda} \rangle$ and $\langle \dot{\phi} \rangle$ may be found in work by *Fok et al.* [1995] and *Fok and Moore* [1997].

[21] The second step is to calculate the FAC, $J_{\|\mathrm{i}}$, in the ionosphere and the ionospheric potential using the RCM scheme (for the details see *Fok et al.* [2001] and *Toffoletto et al.* [2003]):

$$J_{\|\mathrm{i}} = \frac{1}{r_i \cos^2 \lambda} \sum_j \left(\frac{\partial \eta_j}{\partial \lambda} \frac{\partial W_j}{\partial \phi} - \frac{\partial \eta_j}{\partial \phi} \frac{\partial W_j}{\partial \lambda} \right) \quad (2)$$

where W_j is the kinetic energy of a particle with given λ, ϕ, M, and K. η_j is the number of particles per unit magnetic flux associated with ΔM, ΔK:

$$\eta_j = 4\sqrt{2}\pi m_0^{3/2} \bar{f}_s(\lambda, \phi, M, K) M^{1/2} \Delta M \Delta K \quad (3)$$

Having the distribution of FAC, the ionospheric potential is obtained from the Poisson-like equation

$$\nabla \cdot (-\Sigma \cdot \nabla \Phi) = J_{\|\mathrm{i}} \sin I \quad (4)$$

where Φ is the electric field potential, Σ is the ionospheric conductivities tensor (field-line integrated), and I is the magnetic field inclination angle.

[22] A standard CRCM grid is used with 48 × 48 points in ϕ and λ and 35 × 28 points in M and K accordingly.

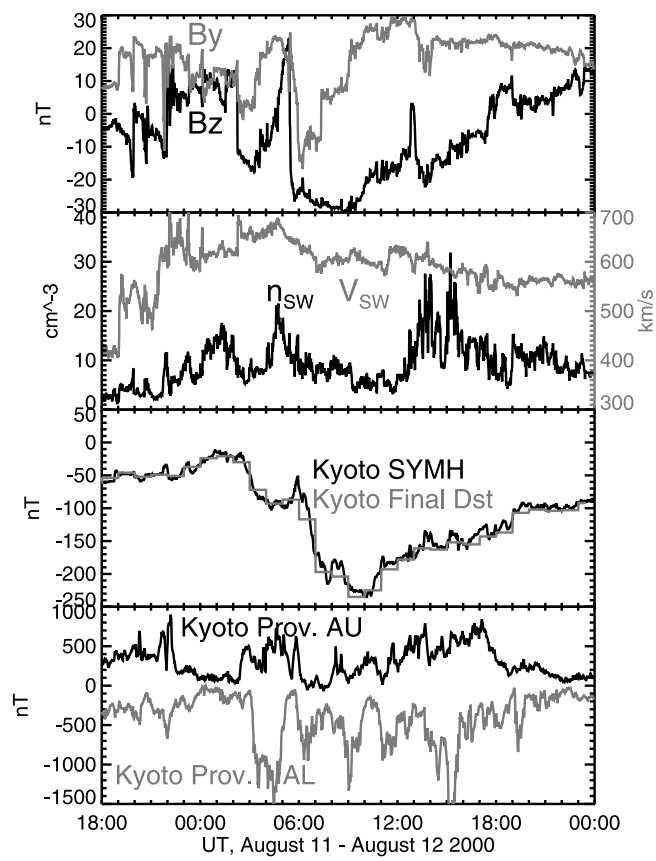

Figure 4. Geomagnetic conditions for 11–12 August 2000. From top to bottom: IMF B_z and B_y (ACE); solar wind density and velocity (ACE); *SYMH* and final *Dst* (Kyoto); and provisional *AU* and *AL* (Kyoto).

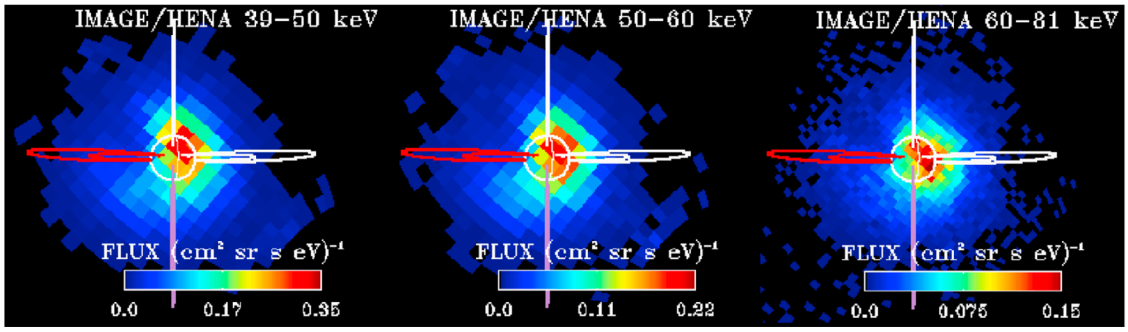

Figure 5. IMAGE/HENA hydrogen ENA flux intensity (/cm^2/sr/s/eV) for 12 August 2000 around 0900 UT in a "fish-eye" projection.

4.2. Input Parameters

[23] The empirical T96 model [*Tsyganenko*, 1995; *Tsyganenko and Stern*, 1996] is used to provide the magnetospheric magnetic field. It is called with static input parameters: $B_z = -10$ nT, $B_y = 0$, Pdyn = 4.5 nPa, $Dst = -50$ nT for 12 August 2000; and $B_z = -3$ nT, $B_y = 0$, Pdyn = 1.7 nPa, $Dst = -30$ nT for 11 October 2008. It is a common practice for CRCM to use a static magnetic field model. It is assumed in this approximation that the main driving force of a storm is the convection electric field and not the time-varying magnetic field.

[24] The polar boundary condition for the electric field potential is calculated from the Weimer-2000 convection model [*Weimer*, 2001] with 5 min averaging of solar wind and IMF data. The density and temperature of the plasma sheet are calculated with the empirical TM2003 model [*Tsyganenko and Mukai*, 2003] at $r = 10\ R_E$ with 30 min averaging for the 12 August 2000 run and 1 h averaging for 11 October 2008. Although TM2003 model has a dependence on MLT, it is minimal near its inner boundary at $r = 10\ R_E$, so the density and temperature are essentially the same for all MLT. The CRCM outer boundary at equatorial SM plane is located at $r = 9\ R_E$ and constant in time.

[25] We consider both H^+ and O^+ ions with O^+/H^+ ratio estimated from *Young et al.* [1982]. For the 11 October 2008 run, we use $n[O^+]/n[H^+] = 1/3$, and for the 12 August 2000 run, we use $n[O^+]/n[H^+] = 1$.

[26] An ionospheric conductivity is calculated as a sum of UV component and an electron precipitation component. The UV component is calculated from The International Reference Ionosphere (IRI-95) [*Bilitza*, 1997] and the Mass Spectrometer Incoherent Scatter (MSISE90) model [*Hedin*, 1991]. These models require day of year, $F_{10.7}$ index, and *Ap* index as input parameters. The electron precipitation component is calculated from the empirical model of *Hardy et al.* [1987] which depends only on the *Kp* index. To calculate the UV component, we use $F_{10.7} = 189 \cdot 10^4$ Jy, $Ap = 123$ for 12 August 2000 and $F_{10.7} = 71 \cdot 10^4$ Jy, $Ap = 37$ for 11 October 2008. Although the CRCM assumes symmetry between grids in two hemispheres, a seasonal dependence of conductivity is included in IRI-95 model.

[27] These input parameters are used for the two reference runs (1800 UT on 11 August 2000 to 2400 UT on 12 August 2000 and 0000–2400 UT on 11 October 2008). Several additional runs for the same events are performed with other inputs to highlight particular effects under examination. Sections 7 and 8 outline the results for each effect examined.

4.3. ENA Calculations

[28] We consider only optically thin hydrogen ENA emissions from the RC, although the CRCM calculates both H^+ and O^+ fluxes. The ENA intensity at an energy E can be obtained from a line of sight integral [*Roelof*, 1987]:

$$j_{\mathrm{ENA}}(E) = \sigma_{\mathrm{H^+,H}}(\mathrm{E}) \int \mathrm{n_H} j_{\mathrm{H^+}}(E, \alpha) dr \qquad (5)$$

where $\sigma_{\mathrm{H^+,\ H}}(E)$ is the charge-exchange cross section; $\mathrm{n_H}$ is the geocoronal H density; $j_{\mathrm{H^+}}(E, \alpha)$ is the H^+ intensity; and, α is the local pitch angle. Only the H^+-H reaction is considered here. For the charge-exchange cross section, we use the relation from *Barnett et al.* [1990]. For the geocoronal density, we use the model of *Rairden et al.* [1986]. Line of sight integrals are calculated for a number of vantage points corresponding to the locations of the IMAGE, TWINS 1/2, or virtual spacecraft.

4.4. Dessler-Parker-Sckopke (DPS) Relation

[29] The Dessler-Parker-Sckopke (DPS) relation [*Dessler and Parker*, 1959; *Sckopke*, 1966; *Carovillano and Siscoe*, 1973] is used to estimate the *Dst**(*SYMH**) indices from RC energy:

$$Dst^*\left(SYMH^*\right)(nT) = -3.98 \cdot 10^{-30} \cdot E_{\mathrm{RC}}(keV) \qquad (6)$$

The pressure correction given by *Gonzalez et al.* [1994] is used to convert *Dst*(*SYMH*) to *Dst**(*SYMH**) with the divisor 1.5 to account for the effect of shielding currents: $Dst^* = Dst/1.5 - c_1 P_{SW}^{1/2} + c_2$ where P_{SW} is a SW dynamic pressure and c_1, c_2 are empirical coefficients with values of 0.2 nT/(eV cm^{-3})$^{1/2}$ and 20 nT, respectively. When calculating RC energy, we consider both H^+ and O^+ species inside the modeled region (i.e., inside equatorial boundary $r = 9\ R_E$).

[30] Despite the limitations (nondipole magnetic field used in the CRCM, possible errors in pressure correction terms, neglecting magnetic energy of RC), the DPS relation

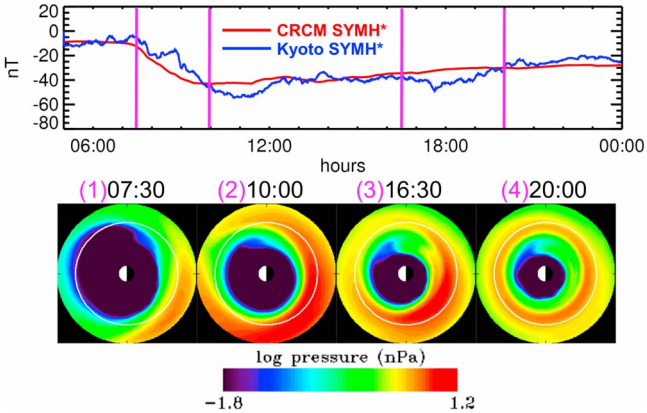

Figure 6. (top) Comparison of Kyoto *SYMH** index with CRCM-calculated *SYMH** for 11 October 2008. (bottom) Ring current pressure distribution (1–180 keV; H^+ and O^+).

is a simple, powerful tool for describing RC dynamics and storm strength.

5. Results for the 11 October 2008 Storm

[31] Figure 6 shows the comparison of CRCM-calculated *SYMH** index with Kyoto-corrected *SYMH** index. The bottom panel also shows RC pressure calculated from the CRCM in the energy range from 1 to 180 keV for several times. Both H^+ and O^+ components are included in calculation of *SYMH** and RC pressure. The modeled *SYMH** is smoother than the Kyoto *SYMH**, due to the use of static magnetic field and averaged SW/IMF data as CRCM inputs. The overall agreement is quite reasonable. The pressure plots show the 'classic' behavior of the RC. The RC is weak and asymmetric at the beginning of the storm, and strong and asymmetric during the main phase of the storm. The RC becomes symmetric in the late recovery phase with a smooth transition from asymmetric to symmetric during the first ~9 h of the recovery phase. During the main phase, a significant part of the RC is located outside geostationary orbit.

[32] The RC pressure peaks in the dusk sector during the main phase. To see how the RC asymmetry is reflected in ENA emissions, we plot CRCM-simulated H ENA emissions for 1030 UT to compare with TWINS data.

[33] The first column of Figure 7 shows the TWINS 1/2 flux intensities around 1030 UT for 8 and 12 keV (assuming hydrogen ENA). The color scale is linear. The second column shows CRCM simulated hydrogen ENA (H ENA) for TWINS 1/2 at 1030 UT for the same energies. The color scale for the second column has a different maximum value than the TWINS plots. The third column shows ENA fluxes calculated from the same vantage point as the second column but with an isotropic pitch angle distribution (PAD). We calculate ENA emissions with an isotropic PAD to show the effect of RC anisotropy. The equatorial flux intensity used to calculate isotropic PAD is the same as for the nonisotropic PAD.

[34] A PME is seen in the modeled ENA emissions both at 8 keV and 12 keV. CRCM ENA for 12 keV are smaller than for 8 keV; this is similar to what is seen in TWINS data. CRCM-simulated emissions at high altitudes are located at larger radial distances than TWINS emissions. We explain this by substorm activity around ~0815 UT and the consequent substorm injection, which is not described in the CRCM (see also section 9).

[35] CRCM ENA with isotropic PAD reproduce a region with enhanced emissions near the Earth which is seen in TWINS data. These CRCM ENA emissions come from a transition region between LA emissions and high-altitude RC emission where the geocoronal density is higher. This indicates that real PAD are more isotropic. The CRCM does not take into account all processes that control the RC anisotropy, and specifically, act to isotropize RC ions. For example, EMIC waves generated by the RC should lead to isotropization of the distribution function, but this process is not currently included into the CRCM. CRCM-simulated emissions show reasonable agreement with the TWINS RC emissions (here we note again that the CRCM can describe only optically thin RC emissions, so LA emissions cannot be correctly reproduced by the model).

[36] To study the relationship between the RC ENA and equatorial H^+ flux intensity, we plot ENA emissions from a vantage point directly above the magnetic pole in Figure 8. The first column of Figure 8 shows CRCM H ENA emissions calculated from the vantage point at XSM = 0, YSM = 0, ZSM = 6.6 R_E. The viewing direction is toward to the center of the Earth. The Sun is located to the left of the image. The second column shows CRCM-calculated equatorial pitch angle–averaged H^+ flux intensities for 5.7–10.4 keV, 10.4–15.9 keV, 15.9–25.5 keV, and 25.5–38 keV. These particular energy ranges are chosen because they show changes in MLT location of flux peak. The third column of Figure 8 shows perpendicular H^+ partial pressure for these energy ranges. The fourth column of Figure 8 shows ENA fluxes calculated with isotropic PAD. The equatorial flux intensity used to calculate isotropic PAD is the same as shown on the second column (1030 UT on 11 October 2008, pitch angle–averaged flux). The color scales are linear for ENA fluxes and equatorial fluxes, and logarithmic for partial pressure. The outer CRCM boundary is located at 9 R_E in the equatorial plane; a white circle shows the location of geostationary orbit.

[37] As shown from the polar vantage point in Figure 8, simulated PME in the ENA are seen at 8 keV and 12 keV. They shift to dusk at energies of 20 keV and 33 keV. Similar behavior is found for equatorial fluxes and pressure. The location of flux/pressure peak is shifted toward the dusk sector at higher energies. This is what we expect from drift physics; that is, higher energies tend to move westward due to gradient and curvature drifts.

[38] The ENA flux intensity monotonically decreases with energy, while the partial pressure has a peak at energies of 16–38 keV (decreasing at higher energies, not shown here). The relationship between the ENA flux and the equatorial flux is nonlinear. For example, the peak ENA flux for 8 keV (first row, Figure 8) is ~0.4 $(cm^2\ sr\ s\ eV)^{-1}$ and the peak ENA flux for 33 keV is ~0.04 $(cm^2\ sr\ s\ eV)^{-1}$, while maximum values for equatorial H^+ fluxes are approximately the same (flux scales are not saturated). This is because the

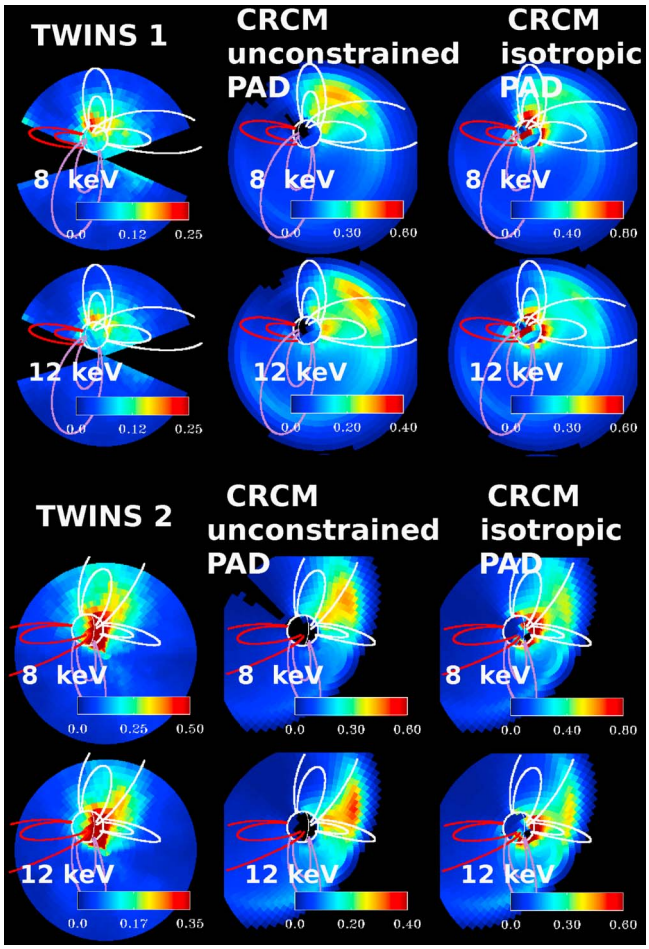

Figure 7. TWINS-CRCM data-model comparison for 11 October 2008 storm main phase. TWINS 1 and TWINS 2 H ENA flux intensity (first column, /cm^2/sr/s/eV); CRCM H ENA flux intensity (second column, /cm^2/sr/s/eV); and CRCM H ENA flux intensity calculated assuming isotropic PAD (third column, /cm^2/sr/s/eV). TWINS 1 and TWINS 2 H ENA are taken around 1030 UT. CRCM H ENA are calculated for 1030 UT. The color scale is linear.

H^+–H charge-exchange cross section falls abruptly (roughly 1 order of magnitude) in the energy range between 10 and 50 keV [e.g., *Lindsay and Stebbings*, 2005]. Most ENA are confined below 16 keV and form PME. The bulk of pressure is in the energy range 16–38 keV and located in premidnight sector.

[39] ENA emissions from the polar vantage point come from two spatially separated regions. The first region is located near the Earth, and the second region is located at ~5–7 R_E. This is explained by an interplay between the thickness of region with intense flux and the region of high geocoronal density. The first region has a smaller thickness of the RC and a higher geocoronal density near the Earth. The second region has a smaller geocoronal density and a thicker near-equatorial region of intense flux. The middle region has a smaller geocoronal density than the first region and a smaller thickness of RC than the second region. As a result a gap in ENA intensity is formed. As activity increases and RC penetrates deeper toward the Earth, these two regions of enhanced ENA production merge into one (see section 6).

6. Results for the 12 August 2000 Storm

[40] Figure 9 shows the comparison of CRCM-calculated *SYMH** index (calculations include contributions from both H^+ and O^+) with Kyoto-corrected *SYMH** index in the same format as Figure 6. The pressure distribution for energies 1–180 keV is shown at the beginning of the storm, main phase, early recovery, and late recovery phase. Similar to the results for the 11 October 2008 event, the RC is highly asymmetric during the main phase/early recovery phase and becomes symmetric during the late recovery phase. When the RC is asymmetric, the pressure peak is located in the dusk-premidnight sector (the same result as obtained for 11 October 2008). Despite these similarities, the RC is confined inside geostationary orbit for 12 August 2000, while a significant portion of RC pressure is located outside geostationary orbit for 11 October 2008. Secondly, during the main phase of 12 August 2000, there is a broad region of enhanced pressure in postmidnight sector. This region is associated with the PME in fluxes and ENA emissions.

[41] Figure 10 shows comparison of IMAGE/HENA data around 0900 UT (first row) with CRCM-simulated H ENA images (second row), pitch angle–averaged equatorial CRCM H^+ fluxes (third row), and corresponding partial pressure (fourth row). The fifth row shows CRCM H ENA emissions calculated for isotropic distributions assuming pitch-averaged flux shown in the third row. For all ENA images, the Sun is located to the left. CRCM ENA are calculated from IMAGE vantage point at XSM = 0.1, YSM = 0.5, XSM = 6.1 R_E. The format of IMAGE/HENA data is the same as Figure 5 but plotted on a logarithmic scale. The same color bar is used for IMAGE/HENA data and CRCM-calculated ENA images in the third row of Figure 10. Similar to 11 October 2008 results, the H ENA intensity falls as energy increases. Again, this is explained by the dependence of charge-exchange cross section on energy. The modeled H ENA emissions (second row of Figure 10) agree reasonably well both in spatial distribution and in intensity with IMAGE/HENA data. There is no significant energy dispersion and the spatial structure of equatorial fluxes (third row of Figure 10) is approximately the same for all three energy bins. The partial pressure reaches its maximum for the highest-energy bin 60–80 keV, while the H ENA intensity reaches its minimum. Most of the H ENA emissions are in the energy range below 60 keV and form a PME (the most intense ENA emissions are seen by IMAGE/HENA at energies below 39 keV and not shown here). Most of the RC pressure is in the energy range above 60 keV. It peaks in dusk-premidnight sector.

[42] There is no separation of ENA emissions into two distributions here as we find for the 11 October 2008 event. This is because the RC penetrates deeply toward the Earth and the gap disappears.

[43] The sixth row of Figure 10 shows the difference between the CRCM ENA map calculated with nonisotropic PAD and the CRCM ENA map calculated with isotropic PAD. Each plot is the CRCM ENA map with anisotropic PAD minus the CRCM ENA map with isotropic PAD. CRCM

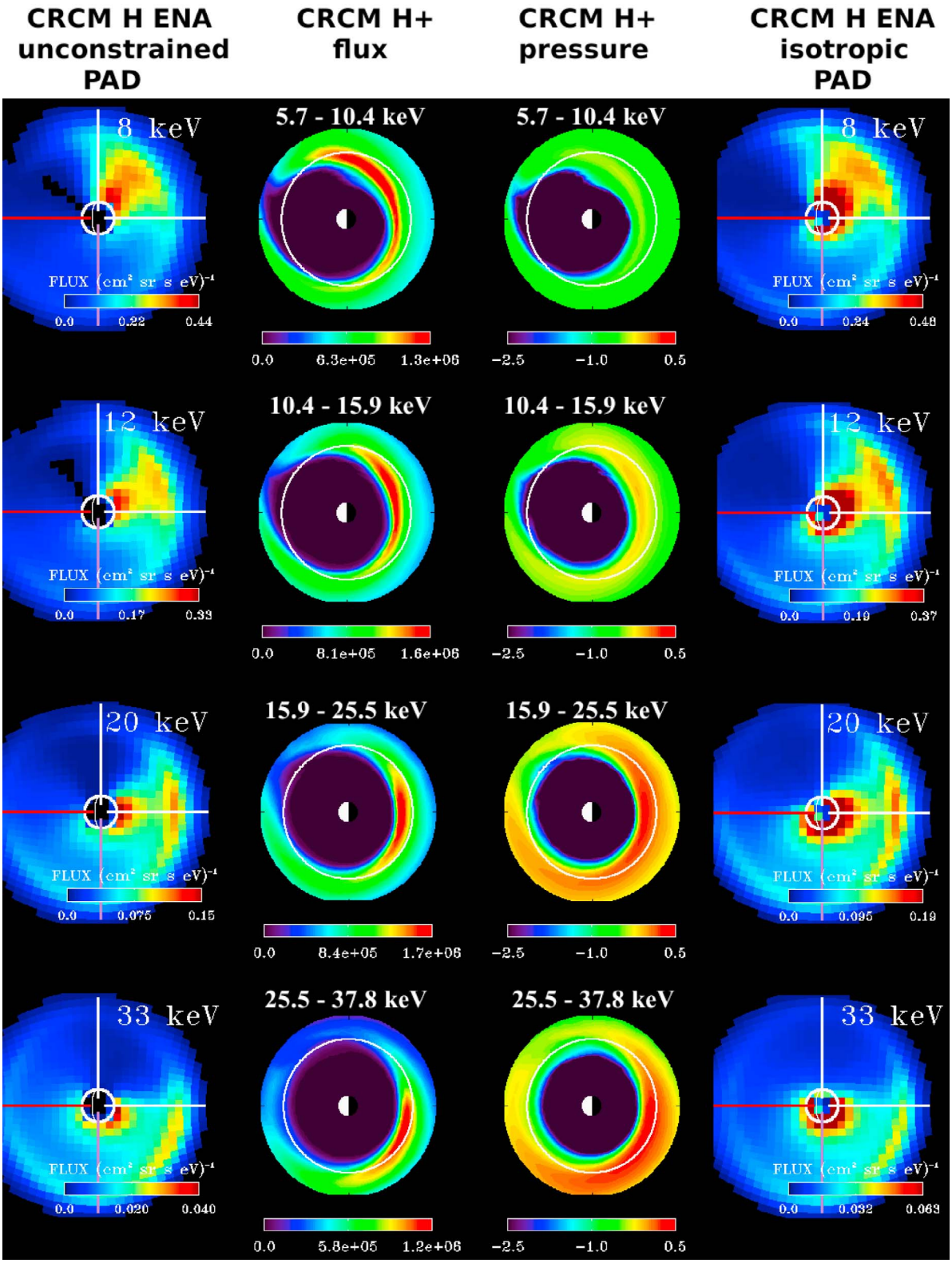

Figure 8. For 1030 UT on 11 October 2008 as would be viewed from a polar vantage point XSM = 0 R_E, YSM = 0 R_E, ZSM = 6.6 R_E: (first column) CRCM-simulated hydrogen ENA flux intensity (/cm^2/sr/s/eV); (second column) pitch angle–averaged equatorial CRCM H^+ flux intensity (/cm^2/sr/s/keV); (third column) corresponding perpendicular partial H^+ pressure (nPa); and (fourth column) CRCM H ENA flux intensity calculated assuming isotropic PAD (/cm^2/sr/s/eV). Equatorial flux distributions for isotropic PAD are shown in the second column. The color scale is linear for ENA flux and equatorial H^+ flux. The color scale for CRCM H^+ pressure is logarithmic.

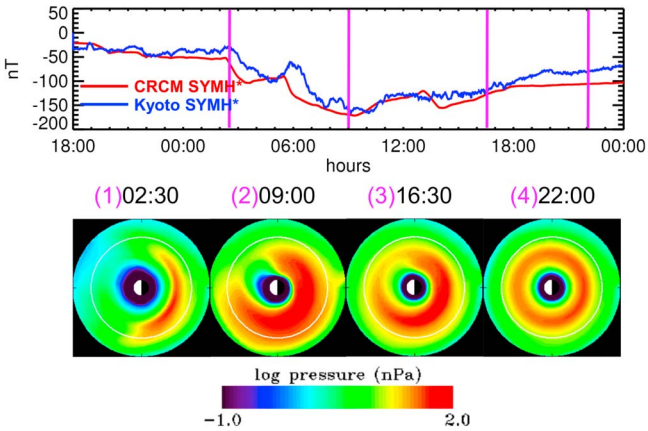

Figure 9. (top) Comparison of Kyoto *SYMH** index with CRCM-calculated *SYMH** for 12 August 2000. (bottom) Ring current pressure distribution (1–180 keV; H^+ and O^+).

ENA emissions calculated with isotropic distribution show a less intense PME as well as a region of enhanced ENA emissions near the Earth. The overall intensity of CRCM ENA emissions for isotropic PAD appears weaker than for the case of CRCM-calculated PAD. The explanation is that the CRCM-calculated PAD is more equatorial (although it has a field-aligned component). It generates relatively strong ENA emissions in the near equatorial region. An isotropic PAD has a smaller number of particles in the near equatorial region and a larger number of particles in the near Earth region. Different PAD with the same number of particles in a magnetic flux tube will lead to different distributions of particles and different ENA emissions. Anisotropic PAD depend on MLT and thus "modulate" ENA emissions, creating MLT regions with weaker/stronger ENA than in the case of isotropic PAD. Although we consider here only optically thin emissions, different PAD will lead to different global distributions of precipitating ions and different LA emissions.

7. IMF B_y Effect on Postmidnight Enhancement

[44] To study the effect of IMF B_y on the formation of PME, we perform two additional CRCM runs for 12 August 2000 and two additional runs for 11 October 2008.

[45] In the first run for 12 August 2000, we change the input for the reference run, setting the IMF B_y = 10 nT for magnetic field model [*Tsyganenko*, 1995; *Tsyganenko and Stern*, 1996]. In the second run for 12 August 2000, we use the reference CRCM setup with B_y = 0 and exclude the IMF B_y effect from the Weimer-2000 convection model. For this purpose a potential drop along the polar CRCM boundary is estimated from the Weimer-2000 model. The CRCM polar boundary conditions for the potential are calculated assuming a sinusoidal dependence in MLT, with a Weimer-derived potential drop. In summary, in the first additional setup, we include the IMF B_y both in the magnetic and the electric field models. In the second additional run, we do not include an IMF B_y. Because the CRCM assumes symmetry between grids in two hemispheres, we assume that inclusion of the IMF B_y effect does not change the grid in the southern hemisphere significantly.

[46] Figure 11 shows CRCM-calculated H ENA emissions for 0900 UT on 12 August 2000 for the two additional CRCM runs described above. The left column shows CRCM H ENA emissions calculated with B_y for 20 keV, 45 keV, 70 keV, 150 keV (from top to bottom) from IMAGE vantage point at XSM = 0.1, YSM = 0.5, ZSM = 6.1 R_E. The right column shows CRCM H ENA emissions calculated without B_y for the same energies. The results demonstrate that CRCM ENA emissions have a clear PME in the energy range 20–70 keV for both runs. However, at each energy level, ENA emissions for the run without B_y are stronger and shifted eastward, making the PME signature more evident. This is explained by the convection electric field strength. Because the Weimer-2000 model produces a skewed convection pattern for B_y near the polar CRCM boundary, exclusion of the IMF B_y effect with the same potential drop results in an electric field with a stronger dawn-dusk component. This means that the effective convection is stronger; the RC energy is larger (not shown here); and the PME is more intense.

[47] The results for 11 October 2008 are shown in Figure 12. In the first run (Figure 12, left column), we use the reference CRCM setup with IMF B_y = 3 nT for magnetic field model. In the second run (Figure 12, right column), we use the reference run with B_y = 0 and excluded B_y from convection model in the same way we do for the 12 August 2000 run. CRCM H ENA are calculated from a polar vantage point at XSM = 0, YSM = 0, ZSM = 6.6 R_E for 8 keV, 12 keV, 20 keV and 45 keV. The strength of these two storms is different and the spectral properties of their PME are different. For example, ENA emissions for 45 keV show PME for strong storm (Figure 11), while for the moderate storm (Figure 12) ENA emissions for 45 keV peak in premidnight sector. However, the IMF B_y effect remains the same for two storms: exclusion of B_y from the convection model makes the effective convection stronger and the PME signature more intense.

8. Convection and Shielding Effect for Moderate and Strong Storms

[48] We have shown that the occurrence of PME at a particular energy depends on both energy and overall storm strength. For strong storms the energy range for PME formation tends to extend to higher energies. The total CRCM-simulated pressure for the strong storm (in the energy range 1–180 keV) has a broad region of enhanced pressure in the postmidnight sector during the main phase (Figure 9, the RC pressure at 0900 UT). The PME is manifested in RC pressure, not only in the low-energy part of RC spectrum as shown for the 11 October 2008 storm. The PME of RC is more evident for the strong storm, although the pressure peak is still located in premidnight sector (Figure 10).

[49] We plot electric field equipotentials (Figure 13) for the main phase of both the strong and the moderate storm at times where ENA measurements are sampled (1030 UT on 11 October 2008 and 0900 UT on 12 August 2000). The electric field for the strong storm is more intense in the inner magnetosphere and the skewing effect is more pronounced. In terms of absolute value, the shielding effect is more

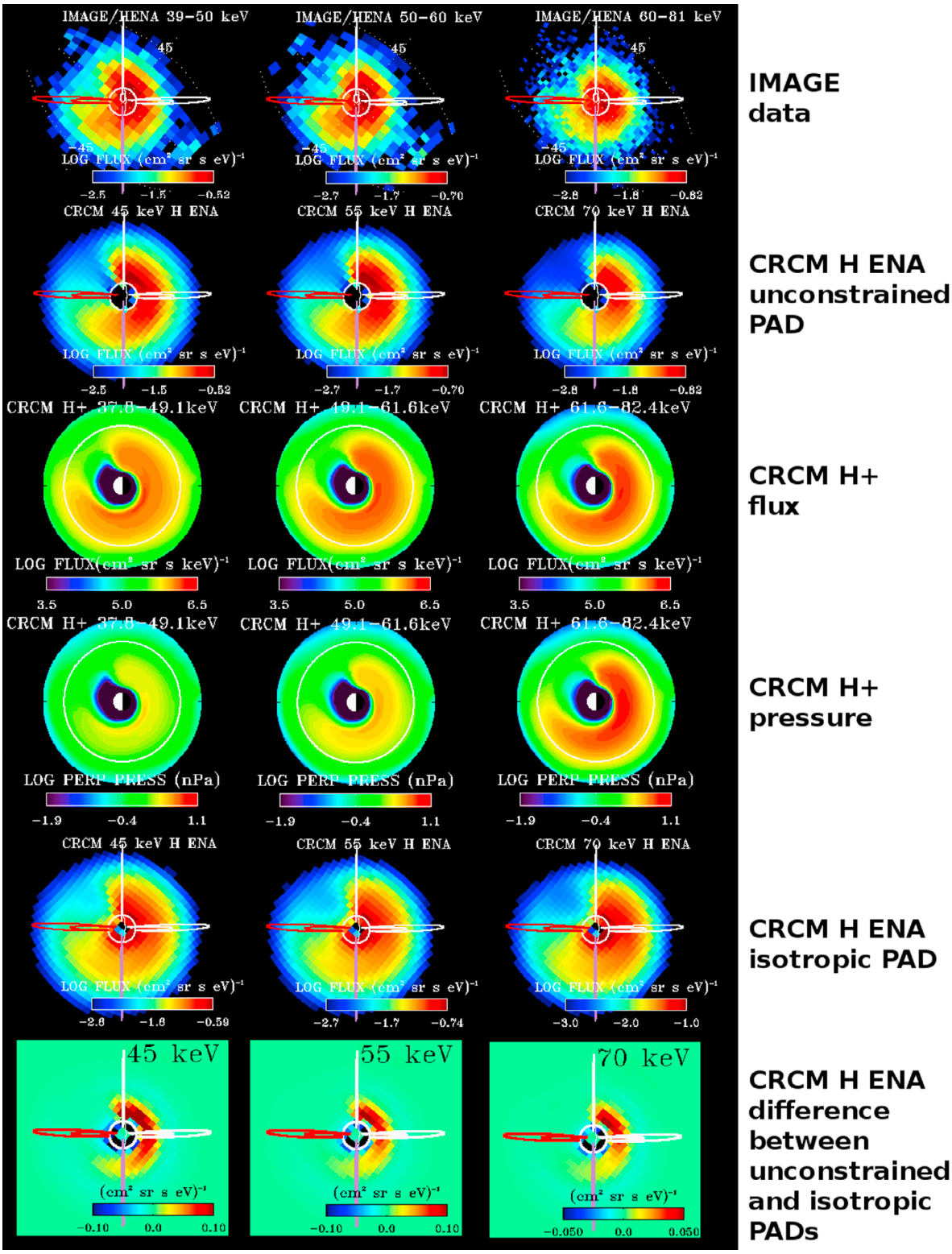

Figure 10. IMAGE/HENA-CRCM data-model comparison for 0900 UT on 12 August 2000 during the storm main phase: (first row) IMAGE/HENA hydrogen ENA flux intensity for three energy bins (/cm^2/sr/s/eV); (second row) CRCM H ENA flux intensity (/cm^2/sr/s/eV); (third row) CRCM pitch angle–averaged equatorial H^+ flux intensity (/cm^2/sr/s/keV); (fourth row) corresponding perpendicular partial H^+ ring current pressure (nPa); (fifth row) CRCM H ENA flux intensity calculated assuming isotropic PAD (/cm^2/sr/s/eV); and (sixth row) difference between CRCM ENA map calculated with anisotropic PAD and CRCM ENA map calculated with isotropic PAD (/cm^2/sr/s/eV). Equatorial flux distributions for isotropic PAD are shown on the third row.

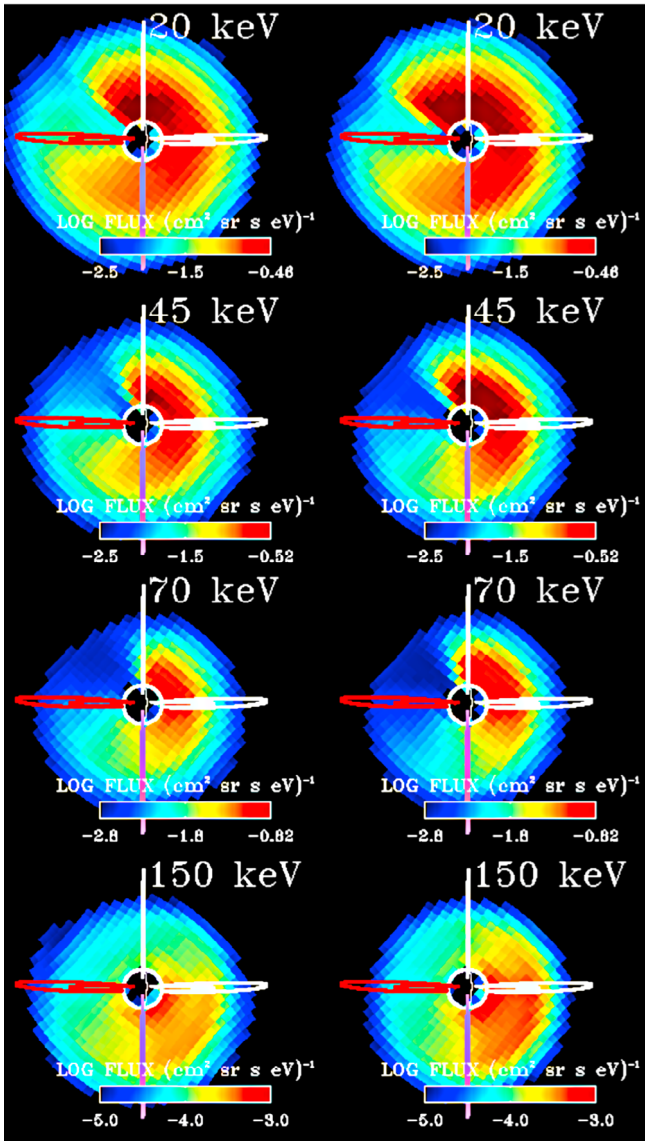

Figure 11. IMF B_y effect on the formation of postmidnight enhancement (PME) for 12 August 2000 (0900 UT). The left column shows CRCM-calculated hydrogen ENA emissions for CRCM run with B_y included. The right column shows hydrogen ENA emissions for CRCM run without B_y (see text for details). ENA emissions are calculated from IMAGE vantage point (XSM = 0.1 R_E, YSM = 0.5 R_E, ZSM = 6.1 R_E).

obvious for the moderate storm. Different convection strengths make it difficult to draw a conclusion as to where the shielding is more effective. To exclude the effect of convection, we perform two additional CRCM runs with the same input parameters but without field-aligned Region II currents (i.e., RC-induced electric fields). These additional runs are similar to the Fok RC model [*Fok et al.*, 1995; *Fok and Moore*, 1997], with the electric field calculated from given ionospheric conductances and polar boundary condition obtained from the Weimer-2000 model. Conductances are time varying but the same for runs with and without RC-induced electric fields. Inside the polar CRCM boundary electric field is calculated in the same way as in the CRCM, but FAC are forced to be zero. The calculated electric field pattern is different from the Weimer-2000 model. Comparing electric field patterns for runs with and without RC-induced electric fields, we are able to isolate and examine the shielding effect.

[50] Figure 14 shows the shielding dependence for the two storms. The shielding coefficient is obtained by calculating the potential drop along the ionospheric latitude $\lambda = 44°$ (L ~ 1.9) for the reference CRCM run and dividing this value by potential drop along the same latitude calculated from the additional CRCM run (without RC-induced electric field). This normalized potential drop, $\Delta\Phi$, describes the effect of RC on the electric field penetrating to low latitudes. Almost the same plots for $\Delta\Phi$ were obtained for $\lambda = 50°$, indicating that there are no sources of electric field at these latitudes.

[51] $\Delta\Phi = 0$ means 'perfect shielding' and $\Delta\Phi = 1$ means a low-latitude potential difference that is the same in the two simulations (i.e., either completely penetrating from high latitudes or rearranged by the RC-induced FAC). Cases with $\Delta\Phi > 1$ correspond to overshielding where the electric field of ring current is stronger than the low-latitude potential difference calculated without RC-induced FAC. Additionally, the Weimer-2000 cross polar cap potential is shown in Figure 14.

[52] There are a number of spikes in $\Delta\Phi$ corresponding to lulls in convection strength, but in general the shielding is well developed for both the strong and moderate storms at $\lambda = 44°$. The shielding factor is ~0.4 for the main phase (0900–1100 UT) of the strong storm, and ~0.2–0.4 for the main phase (0900–1100 UT) of the moderate storm. Magnitudes of potential drop at $\lambda = 44°$ for the moderate storm are 5–10 kV for the base run and 20–30 kV for the run without RC-induced FAC. For the strong storm these values are ~35 kV and ~90 kV, respectively.

[53] Well-developed shielding for the moderate storm indicates relatively large FAC and well-developed skewing of the electric field. However, the absolute value of electric field is higher for the strong storm. This pushes the RC closer to the Earth and creates more pronounced signatures of PME.

[54] The main factors that control shielding are plasma sheet density, temperature, and ionospheric conductivity. High plasma sheet density tends to increase shielding, while high value of ionospheric conductivity and high plasma sheet temperature tend to decrease shielding [*Ebihara et al.*, 2004; *Garner et al.*, 2004; *Ebihara et al.*, 2005]. It is difficult to judge here what factor controls shielding in these particular storms, because all three parameters are different. A separate study is needed to clearly identify what controls shielding in each particular case.

[55] Our results indicate that even relatively well-developed shielding does not entirely cancel the electric field at low latitudes if the outer magnetospheric convection is strong enough. This effect may account for long-lasting penetration electric fields at low latitudes observed during strong storms [*Maruyama et al.*, 2007].

9. Discussion

[56] Previous studies of RC plasma morphology with ENA data [*Brandt et al.*, 2002; *Ebihara and Fok*, 2004;

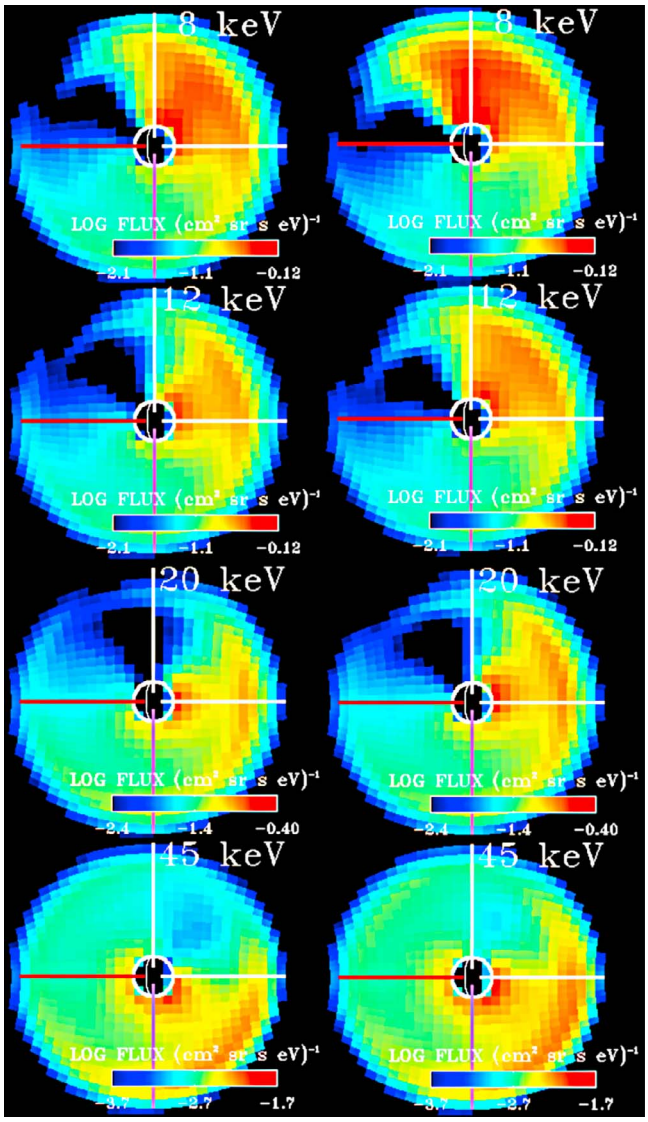

Figure 12. IMF B_y effect on the formation of postmidnight enhancement for 11 October 2008 (1030 UT). The format is the same as for Figure 11. ENA emissions are calculated from a polar vantage point (XSM = 0 R_E, YSM = 0 R_E, ZSM = 6.6 R_E).

Zheng et al., 2006; *Yamauchi et al.*, 2006; *Liemohn et al.*, 2005, 2006] do not concentrate on the energy dependence of PME, although *Brandt et al.* [2002] note that a skewing in ENA is not as strong for the high energies (119–198 keV) as for the lower energies (27–39 keV). *Fok et al.* [2003] study equatorial H^+ fluxes obtained from inversion of MENA/IMAGE and HENA/IMAGE. They obtain PME only for high energies (21.5–44.5 keV), while for low energies (3.8–8.6 keV) no PME is reported. In this case the bulk of the RC pressure should be located in postmidnight sector.

[57] *Denton et al.* [2005] analyze MENA/IMAGE data for 6 keV and 12 keV, and note that the peak in H ENA emissions depends on energy. However, the peak is located near midnight and no PME is reported.

[58] Statistical analysis of Birkeland currents from Iridium [*Anderson et al.*, 2005] show that storm-time dusk currents are shifted to lower latitudes relative to dawn. That is explained by the inflation of the dusk magnetosphere due to the partial RC plasma. Analysis of ground-based magnetometer data [*Shi et al.*, 2006] reveals that during the storm main phase (24 events with $SYMH < -50$ nT) the RC plasma is centered around dusk. To be consistent with findings of *Brandt et al.* [2002], *Shi et al.* [2006] note that a PME should be a short-lived phenomena. On the other hand, *Perez et al.* [2004] study 33 keV H^+ equatorial distributions obtained from inversion of HENA/IMAGE data for 12 August 2000. These inversion results show PME lasting at least 3 h during 1000–1300 UT. Based on analysis of LANL data, *Milillo et al.* [2006] show that during the 21–25 April 2001 storm the postmidnight enhancement of H^+ fluxes is observed during many hours of storm main phase.

[59] Our results are consistent with the findings of *Perez et al.* [2004] and *Milillo et al.* [2006] and indicate that the PME phenomenon is a stable configuration under strong electric field during the main phase/early recovery phase. The bulk of the total RC pressure is formed by the hard part of the RC spectrum and is centered around dusk (consistent with findings of *Le et al.* [2004], *Anderson et al.* [2005], and *Shi et al.* [2006]). Intense PME may be found in the lower energy range. A particular energy range for a PME depends on the particular convection strength and varies from storm to storm. This conclusion explains the difference between studies of magnetic depression maps, in situ particle measurements, and ENA observations.

[60] *Liemohn et al.* [2005] study 39–60 keV IMAGE/HENA data during the recovery phase of the 17 April 2000 storm with $Dst_{\min} = -98$ nT. The RC with energies between 39 and 60 keV is concentrated around midnight, both in data and simulations. No PME is reported. Simulated RC pressure peaks at dusk sector. Our results do not contradict these findings because we show that PME is formed in a particular energy range depending on the strength of the storm. Midnight-centered RC plasma during the recovery phase may be formed as a result of convection weakening. Initially, a PME is formed during the main phase and starts to drift in the westward direction after convection decreases during the recovery phase.

[61] *Ebihara et al.* [2009] show an example (Figure 3) of CRCM-calculated RC pressure and electric field. The pressure peak is located at dusk while strong skewed electric fields are obtained between postmidnight and dawn. This is also consistent with our results: skewed electric fields control the low-energy part of the RC spectra which is responsible for PME formation while pressure peaks at dusk.

[62] *Lui* [2003] and *Lui et al.* [2005] mention that pitch angle anisotropy of RC is important for estimation of ion intensity from ENA emissions. This idea is further developed by *Zheng et al.* [2008] and supported by CRCM-based ENA calculations. One of the results obtained by *Zheng et al.* [2008] is that pitch angle anisotropy is important in determining ENA emissions from different vantage points. Our results extend the findings of *Zheng et al.* [2008]. We find that isotropic PAD significantly enhance ENA emission in the near-Earth transition region between LA ENA emissions and RC ENA emissions. For 12 August 2000, we

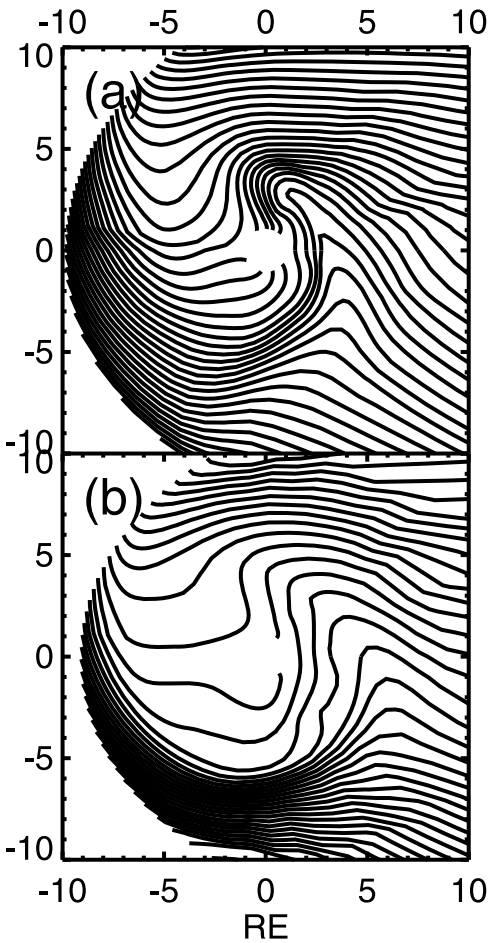

Figure 13. CRCM-calculated electric field equipotentials for the main phases of the strong and moderate storms: (a) 12 August 2000, 0900 UT; (b) 11 October 2008, 1030 UT. Equipotentials have 5 kV spacing for 12 August 2000 and 2 kV spacing for 11 October 2008. Corotation is not included.

determine that CRCM-calculated PAD make PME signatures stronger than those of isotropic PAD.

[63] In this study we use static magnetic field, assuming that the main driving force for a storm is a convection electric field. We neglect the effect of the induction electric field and substorms on RC dynamics. Our results for the 12 August 2000 storm and other studies with the CRCM indicate that the CRCM with static magnetic field adequately describes RC dynamics during storm time conditions, at least for relatively strong events with $Dst_{\min} < -100$ nT [*Fok et al.*, 2001; *Ebihara and Fok*, 2004; *Ebihara et al.*, 2004; *Zheng et al.*, 2006, 2008]. However it is possible that for moderate and small storms a substorm induced electric field may be a main driving force instead convection. For example, the 11 October 2008 event shows a relatively strong intensification of *AL* index at ~0815 UT (Figure 1), indicating on substorm development. The simulated CRCM emissions for 1030 UT appear to be at larger radial distances than TWINS ENA emissions. In this interpretation, TWINS detectors at 1030 UT see the effect of substorm injection. CRCM does not include any substorm induced electric field and cannot describe a substorm injection adequately.

[64] We study how the IMF B_y effect influences PME formation. Although our analysis is limited to only two storms, we find that skewing of the electric field and PME formation is due to RC control of the inner magnetosphere electric field rather than IMF B_y control. *Brandt et al.* [2002] show that PME are observed during storms with strong IMF B_y. Our results do not contradict the findings of *Brandt et al.* [2002] because we obtain PME for CRCM runs with IMF B_y effect included. However, CRCM results indicate that IMF B_y effect is not critical in PME formation. Our findings are consistent with observational evidence that skewing is due to RC-driven electric field distortion rather than B_y twisting [*Burke et al.*, 1998; *Rowland and Wygant*, 1998; *Wygant et al.*, 1998; *Burke et al.*, 2000; *Nishimura et al.*, 2009].

10. Conclusions

[65] Comparing TWINS ENA and IMAGE/HENA data with CRCM model results, we study the ring current characteristics during the main phase of two storms: a strong storm near solar maximum (12 August 2000) and a moderate storm near solar minimum (11 October 2008). The results are summarized as follows.

[66] 1. The CRCM describes the ring current morphology reasonably well: asymmetry during the main phase/early recovery phase; symmetrization in the late recovery phase. The CRCM-calculated *SYMH** index agrees reasonably well with the Kyoto *SYMH** for both storms.

[67] 2. ENA fluxes observed by two different instruments (HENA/IMAGE and TWINS) during two different events agree reasonably well with the CRCM-calculated ENA both in terms of spatial location and flux magnitude. However, we find that for the moderate storm with $Dst_{\min} = -60$ nT the simulated emissions appear to be at larger distances than TWINS emissions. We explain this difference by the effect of a substorm injection which occurred ~2 h before TWINS observations.

[68] 3. We find that the strong storm with $Dst_{\min} = -235$ nT and moderate storm with $Dst_{\min} = -60$ nT have different spectral characteristics of postmidnight enhancement. For both storms, the more intense hydrogen ENA emissions occur in the postmidnight sector, while the bulk of the ring current pressure peaks in the premidnight sector. Most of the ring current hydrogen ENA emissions for the moderate storm are produced by ions with energies below ~16 keV, which peak in the postmidnight sector, while most of the ring current pressure is produced by ions with energies above ~16 keV, which peak in the premidnight sector. For the main phase of the strong storm, most of the hydrogen ENA emissions are produced by ions with energies below ~60 keV, while most of the ring current pressure is produced with ions above ~60 keV. The explanation of the difference between location of pressure peak and ENA peak is based on the dependence of the charge-exchange cross section with energy, which falls about 1 order of magnitude over the energy range from 10 to 50 keV. Because this energy range is critical for ring current, the effect 'masks' most of ring current pressure located in dusk-premidnight sectors.

[69] 4. A skewing of the electric field by the ring current is critical for postmidnight enhancement [*Brandt et al.*, 2002; *Ebihara and Fok*, 2004]. The skewing is stronger when field-aligned currents are stronger. Strong field-aligned

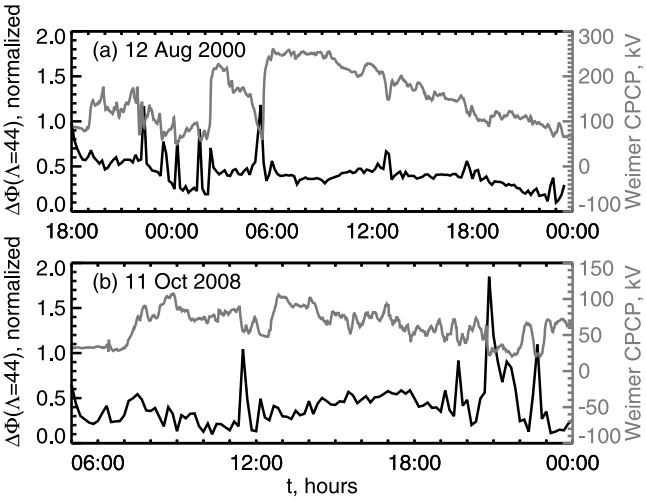

Figure 14. Shielding effect during two storms: (a) 12 August 2000 and (b) 11 October 2008. The black line on each panel shows the CRCM-calculated potential drop ($\Delta\Phi$) along an ionospheric latitude $\lambda = 44°$ (L ~ 1.9) normalized to the value of the potential drop along the same latitude but without the effect of ring current–induced electric field (see text for details). The grey line shows the Weimer-2000 cross polar cap potential (CPCP).

currents also generate the shielding effect. We find that relative shielding and hence electric field skewing is well developed for both events. For the formation of postmidnight enhancement, both the skewing effect and the existence of strong convection are important. If the convection is strong enough, an intense electric field could exist in the inner magnetosphere despite the shielding. An intense electric field during the main phase will push particles closer to the Earth and create more pronounced postmidnight enhancement. This intense electric field may account for the long-lasting penetration of magnetospheric electric field observed during strong storms [e.g., *Maruyama et al.*, 2007].

[70] 5. Our CRCM results show that the IMF B_y effect (twisting of the convection pattern due to B_y) is not needed to form a postmidnight enhancement, at least in terms of the electric and magnetic field models adopted in the CRCM. The more important factors are the overall convection strength and electric field skewing due to the shielding effect. Although our analysis is made for only two storms, this result is consistent with observational evidence that skewing is due to ring current driven electric field distortion rather than B_y twisting.

[71] 6. The pitch angle anisotropy also plays a role in the formation of ENA postmidnight enhancement as was suggested by *Lui* [2003]. In general, having the same number of particles within a magnetic flux tube, the ring current ENA emissions and low-altitude ENA emissions should be different for different PAD. For the case of an isotropic PAD, more intense optically thin ring current ENA emissions occur near the Earth in the transition region between high-altitude emissions and exospheric low-altitude emissions. A more field-aligned PAD at a particular MLT should lead to stronger ENA emissions because the charge-exchange occurs closer to the Earth, where the geocoronal density is higher. In particular, we find that for the 12 August 2000 storm CRCM-calculated PAD produce clearer signatures of postmidnight enhancement than isotropic PAD.

[72] **Acknowledgments.** We thank the TWINS team for a lot of discussions and fruitful comments. The computer programs to calculate ionospheric conductivities and solve for the electrostatic potential were written by R. Spiro and S. Sazykin. *Dst*, *AU*/*AL*, and *SYMH* indices were provided by the World Data Center for Geomagnetism, Kyoto. ACE SW and IMF data were obtained from the GSFC/SPDF OMNIWeb interface at http://omniweb.gsfc.nasa.gov. This work was supported by the TWINS mission, which is a part of NASA's Explorers Program, and NASA Heliophysics Guest Investigators Program, under Work Breakdown Structure 955518.02.01.02.57. For N.B., this work was supported by an appointment to the NPP at the NASA Goddard Space Flight Center administered by ORAU through a contract with NASA and by an appointment at the NASA Goddard Space Flight Center administered by CRESST/UMD through a contract with NASA. N.B. thanks A. Glocer and E. Mitchell for proofreading of the manuscript.

[73] Masaki Fujimoto thanks the reviewers for their assistance in evaluating this paper.

References

Anderson, B. J., S. Ohtani, H. Korth, and A. Ukhorskiy (2005), Storm time dawn-dusk asymmetry of the large-scale Birkeland currents, *J. Geophys. Res.*, *110*, A12220, doi:10.1029/2005JA011246.

Barnett, C. F., H. T. Hunter, M. I. Fitzpatrick, I. Alvarez, C. Cisneros, and R. A. Phaneuf (1990), Atomic data for fusion. Volume 1: Collisions of H, H_2, He and Li atoms and ions with atoms and molecules, *NASA STI/Recon Tech. Rep.*, *91*, A22–A23.

Bazell, D., H. Nair, E. Roelof, T. Sotirelis, P. Brandt, P. Valek, J. Goldstein, D. McComas, and J. Redfern (2010), TWINS 1/2 ENA images of low-altitude emission: Comparison with in situ DMSP measurements of precipitating ions, *J. Geophys. Res.*, *115*, A10204, doi:10.1029/2010JA015644.

Bilitza, D. (1997), International reference ionosphere-status 1995/96, *Adv. Space Res.*, *20*, 1751–1754, doi:10.1016/S0273-1177(97)00584-X.

Brandt, P. C., S. Ohtani, D. G. Mitchell, M.-C. Fok, E. C. Roelof, and R. Demajistre (2002), Global ENA observations of the storm mainphase ring current: Implications for skewed electric fields in the inner magnetosphere, *Geophys. Res. Lett.*, *29*(20), 1954, doi:10.1029/2002GL015160.

Burke, W. J., N. C. Maynard, M. P. Hagan, R. A. Wolf, G. R. Wilson, L. C. Gentile, M. S. Gussenhoven, C. Y. Huang, T. W. Garner, and F. J. Rich (1998), Electrodynamics of the inner magnetosphere observed in the dusk sector by CRRES and DMSP during the magnetic storm of June 4–6, 1991, *J. Geophys. Res.*, *103*, 29,399–29,418, doi:10.1029/98JA02197.

Burke, W. J., A. G. Rubin, N. C. Maynard, L. C. Gentile, P. J. Sultan, F. J. Rich, O. de La Beaujardière, C. Y. Huang, and G. R. Wilson (2000), Ionospheric disturbances observed by DMSP at middle to low latitudes during the magnetic storm of June 4–6, 1991, *J. Geophys. Res.*, *105*, 18,391–18,406, doi:10.1029/1999JA000188.

Burton, R. K., R. L. McPherron, and C. T. Russell (1975), An empirical relationship between interplanetary conditions and *Dst*, *J. Geophys. Res.*, *80*, 4204–4214, doi:10.1029/JA080i031p04204.

Buzulukova, N., M. C. Fok, A. Pulkkinen, M. Kuznetsova, T. E. Moore, A. Glocer, and L. Rastätter (2010), Dynamics of ring current and electric fields in the inner magnetosphere during disturbed periods: CRCM–BATS-R-US coupled model, *J. Geophys. Res.*, *115*, A05210, doi:10.1029/2009JA014621.

Carovillano, R. L., and G. L. Siscoe (1973), Energy and momentum theorems in magnetospheric processes, *Rev. Geophys.*, *11*, 289–353, doi:10.1029/RG011i002p00289.

Denton, M. H., V. K. Jordanova, M. G. Henderson, R. M. Skoug, M. F. Thomsen, C. J. Pollock, S. Zaharia, and H. O. Funsten (2005), Storm-time plasma signatures observed by IMAGE/MENA and comparison with a global physics-based model, *Geophys. Res. Lett.*, *32*, L17102, doi:10.1029/2005GL023353.

Dessler, A. J., and E. N. Parker (1959), Hydromagnetic theory of geomagnetic storms, *J. Geophys. Res.*, *64*, 2239–2252, doi:10.1029/JZ064i012p02239.

Ebihara, Y., and M.-C. Fok (2004), Postmidnight storm-time enhancement of tens-of-keV proton flux, *J. Geophys. Res.*, *109*, A12209, doi:10.1029/2004JA010523.

Ebihara, Y., M. Ejiri, H. Nilsson, I. Sandahl, A. Milillo, M. Grande, J. F. Fennell, and J. L. Roeder (2002), Statistical distribution of the storm-time

proton ring current: POLAR measurements, *Geophys. Res. Lett.*, *29*(20), 1969, doi:10.1029/2002GL015430.

Ebihara, Y., M.-C. Fok, R. A. Wolf, T. J. Immel, and T. E. Moore (2004), Influence of ionosphere conductivity on the ring current, *J. Geophys. Res.*, *109*, A08205, doi:10.1029/2003JA010351.

Ebihara, Y., M. Fok, R. A. Wolf, M. F. Thomsen, and T. E. Moore (2005), Nonlinear impact of plasma sheet density on the storm-time ring current, *J. Geophys. Res.*, *110*, A02208, doi:10.1029/2004JA010435.

Ebihara, Y., N. Nishitani, T. Kikuchi, T. Ogawa, K. Hosokawa, M. Fok, and M. F. Thomsen (2009), Dynamical property of storm time subauroral rapid flows as a manifestation of complex structures of the plasma pressure in the inner magnetosphere, *J. Geophys. Res.*, *114*, A01306, doi:10.1029/2008JA013614.

Fok, M.-C., and T. E. Moore (1997), Ring current modeling in a realistic magnetic field configuration, *Geophys. Res. Lett.*, *24*, 1775–1778, doi:10.1029/97GL01255.

Fok, M.-C., T. E. Moore, J. U. Kozyra, G. C. Ho, and D. C. Hamilton (1995), Three-dimensional ring current decay model, *J. Geophys. Res.*, *100*, 9619–9632, doi:10.1029/94JA03029.

Fok, M.-C., R. A. Wolf, R. W. Spiro, and T. E. Moore (2001), Comprehensive computational model of Earth's ring current, *J. Geophys. Res.*, *106*, 8417–8424, doi:10.1029/2000JA000235.

Fok, M.-C., et al. (2003), Global ENA image simulations, *Space Sci. Rev.*, *109*, 77–103, doi:10.1023/B:SPAC.0000007514.56380.fd.

Garner, T. W., R. A. Wolf, R. W. Spiro, W. J. Burke, B. G. Fejer, S. Sazykin, J. L. Roeder, and M. R. Hairston (2004), Magnetospheric electric fields and plasma sheet injection to low L-shells during the 4–5 June 1991 magnetic storm: Comparison between the Rice Convection Model and observations, *J. Geophys. Res.*, *109*, A02214, doi:10.1029/2003JA010208.

Gonzalez, W. D., J. A. Joselyn, Y. Kamide, H. W. Kroehl, G. Rostoker, B. T. Tsurutani, and V. M. Vasyliunas (1994), What is a geomagnetic storm?, *J. Geophys. Res.*, *99*, 5771–5792, doi:10.1029/93JA02867.

Hardy, D. A., M. S. Gussenhoven, R. Raistrick, and W. J. McNeil (1987), Statistical and functional representations of the pattern of auroral energy flux, number flux, and conductivity, *J. Geophys. Res.*, *92*, 12,275–12,294, doi:10.1029/JA092iA11p12275.

Harel, M., R. A. Wolf, P. H. Reiff, R. W. Spiro, W. J. Burke, F. J. Rich, and M. Smiddy (1981), Quantitative simulation of a magnetospheric substorm: 1. Model logic and overview, *J. Geophys. Res.*, *86*, 2217–2241, doi:10.1029/JA086iA04p02217.

Hedin, A. E. (1991), Extension of the MSIS thermosphere model into the middle and lower atmosphere, *J. Geophys. Res.*, *96*, 1159–1172, doi:10.1029/90JA02125.

Jaggi, R. K., and R. A. Wolf (1973), Self-consistent calculation of the motion of a sheet of ions in the magnetosphere, *J. Geophys. Res.*, *78*, 2852–2866, doi:10.1029/JA078i016p02852.

Jorgensen, A. M., H. E. Spence, W. J. Hughes, and H. J. Singer (2004), A statistical study of the global structure of the ring current, *J. Geophys. Res.*, *109*, A12204, doi:10.1029/2003JA010090.

Lavraud, B., V. K. Jordanova, and M. F. Thomsen (2008), Modeling the effects of local time variation of plasma sheet properties on proton ring current energy and peak location, *J. Geophys. Res.*, *113*, A05215, doi:10.1029/2007JA012883.

Le, G., C. Russell, and K. Takahashi (2004), Morphology of the ring current derived from magnetic field observations, *Ann. Geophys.*, *22*, 1267–1295.

Liemohn, M. W., A. J. Ridley, P. C. Brandt, D. L. Gallagher, J. U. Kozyra, D. M. Ober, D. G. Mitchell, E. C. Roelof, and R. DeMajistre (2005), Parametric analysis of nightside conductance effects on inner magnetospheric dynamics for the 17 April 2002 storm, *J. Geophys. Res.*, *110*, A12S22, doi:10.1029/2005JA011109.

Liemohn, M. W., A. J. Ridley, J. U. Kozyra, D. L. Gallagher, M. F. Thomsen, M. G. Henderson, M. H. Denton, P. C. Brandt, and J. Goldstein (2006), Analyzing electric field morphology through data-model comparisons of the Geospace Environment Modeling Inner Magnetosphere/Storm Assessment Challenge events, *J. Geophys. Res.*, *111*, A11S11, doi:10.1029/2006JA011700.

Lindsay, B. G., and R. F. Stebbings (2005), Charge transfer cross sections for energetic neutral atom data analysis, *J. Geophys. Res.*, *110*, A12213, doi:10.1029/2005JA011298.

Lui, A. T. Y. (2003), Inner magnetospheric plasma pressure distribution and its local time asymmetry, *Geophys. Res. Lett.*, *30*(16), 1846, doi:10.1029/2003GL017596.

Lui, A. T. Y., P. C. Brandt, and D. G. Mitchell (2005), Observations of energetic neutral oxygen by IMAGE/HENA and Geotail/EPIC, *Geophys. Res. Lett.*, *32*, L13104, doi:10.1029/2005GL022851.

Maruyama, N., et al. (2007), Modeling storm-time electrodynamics of the low-latitude ionosphere thermosphere system: Can long lasting disturbance electric fields be accounted for?, *J. Atmos. Sol. Terr. Phys.*, *69*, 1182–1199, doi:10.1016/j.jastp.2006.08.020.

McComas, D. J., et al. (2009), The Two Wide-Angle Imaging Neutral-Atom Spectrometers (TWINS) NASA Mission-of-Opportunity, *Space Sci. Rev.*, *142*, 157–231, doi:10.1007/s11214-008-9467-4.

Milillo, A., S. Orsini, S. Massetti, and A. Mura (2006), Geomagnetic activity dependence of the inner magnetospheric proton distribution: An empirical approach for the 21–25 April 2001 storm, *J. Geophys. Res.*, *111*, A11S13, doi:10.1029/2006JA011956.

Nishimura, Y., T. Kikuchi, J. Wygant, A. Shinbori, T. Ono, A. Matsuoka, T. Nagatsuma, and D. Brautigam (2009), Response of convection electric fields in the magnetosphere to IMF orientation change, *J. Geophys. Res.*, *114*, A09206, doi:10.1029/2009JA014277.

Perez, J. D., X. Zhang, P. C:son Brandt, D. G. Mitchell, J. Jahn, and C. J. Pollock (2004), Dynamics of ring current ions as obtained from IMAGE HENA and MENA ENA images, *J. Geophys. Res.*, *109*, A05208, doi:10.1029/2003JA010164.

Rairden, R. L., L. A. Frank, and J. D. Craven (1986), Geocoronal imaging with Dynamics Explorer, *J. Geophys. Res.*, *91*, 13,613–13,630, doi:10.1029/JA091iA12p13613.

Roelof, E. C. (1987), Energetic neutral atom image of a storm-time ring current, *Geophys. Res. Lett.*, *14*, 652–655, doi:10.1029/GL014i006p00652.

Rowland, D. E., and J. R. Wygant (1998), Dependence of the large-scale, inner magnetospheric electric field on geomagnetic activity, *J. Geophys. Res.*, *103*, 14,959–14,964, doi:10.1029/97JA03524.

Sckopke, N. (1966), A general relation between the energy of trapped particles and the disturbance field near the Earth, *J. Geophys. Res.*, *71*, 3125–3130.

Shi, Y., E. Zesta, L. R. Lyons, K. Yumoto, and K. Kitamura (2006), Statistical study of effect of solar wind dynamic pressure enhancements on dawn-to-dusk ring current asymmetry, *J. Geophys. Res.*, *111*, A10216, doi:10.1029/2005JA011532.

Toffoletto, F., S. Sazykin, R. Spiro, and R. Wolf (2003), Inner magnetospheric modeling with the Rice Convection Model, *Space Sci. Rev.*, *107*, 175–196, doi:10.1023/A:1025532008047.

Tsyganenko, N. A. (1995), Modeling the Earth's magnetospheric magnetic field confined within a realistic magnetopause, *J. Geophys. Res.*, *100*, 5599–5612, doi:10.1029/94JA03193.

Tsyganenko, N. A., and T. Mukai (2003), Tail plasma sheet models derived from Geotail particle data, *J. Geophys. Res.*, *108*(A3), 1136, doi:10.1029/2002JA009707.

Tsyganenko, N. A., and D. P. Stern (1996), Modeling the global magnetic field of the large-scale Birkeland current systems, *J. Geophys. Res.*, *101*, 27,187–27,198, doi:10.1029/96JA02735.

Weimer, D. R. (2001), An improved model of ionospheric electric potentials including substorm perturbations and application to the Geospace Environment Modeling November 24, 1996, event, *J. Geophys. Res.*, *106*, 407–416, doi:10.1029/2000JA000604.

Wygant, J., D. Rowland, H. J. Singer, M. Temerin, F. Mozer, and M. K. Hudson (1998), Experimental evidence on the role of the large spatial scale electric field in creating the ring current, *J. Geophys. Res.*, *103*, 29,527–29,544, doi:10.1029/98JA01436.

Yamauchi, M., et al. (2006), Source location of the wedge-like dispersed ring current in the morning sector during a substorm, *J. Geophys. Res.*, *111*, A11S09, doi:10.1029/2006JA011621.

Young, D. T., H. Balsiger, and J. Geiss (1982), Correlations of magnetospheric ion composition with geomagnetic and solar activity, *J. Geophys. Res.*, *87*, 9077–9096, doi:10.1029/JA087iA11p09077.

Zheng, Y., A. T. Y. Lui, M. Fok, B. J. Anderson, P. C. Brandt, T. J. Immel, and D. G. Mitchell (2006), Relationship between Region 2 field-aligned current and the ring current: Model results, *J. Geophys. Res.*, *111*, A11S06, doi:10.1029/2006JA011603.

Zheng, Y., A. T. Y. Lui, and M. Fok (2008), Viewing perspective in energetic neutral atom intensity, *J. Geophys. Res.*, *113*, A09217, doi:10.1029/2008JA013070.

P. C. Brandt, Applied Physics Laboratory, Johns Hopkins University, 11100 Johns Hopkins Rd., Laurel, MD 20723-6099, USA.

N. Buzulukova and M.-C. Fok, NASA Goddard Space Flight Center, Mail Code 673, 8800 Greenbelt Rd., Greenbelt, MD 20771, USA. (nbuzulukova@gmail.com)

J. Goldstein, D. J. McComas, and P. Valek, Space Science and Engineering Division, Southwest Research Institute, 6220 Culebra Rd., San Antonio, TX 78228-0510, USA.